Dalton Transactions

ROYAL SOCIETY OF CHEMISTRY

COMMUNICATION

View Article Online
View Journal | View Issue

Cite this: *Dalton Trans.*, 2024, **53**, 2456

Received 27th September 2023,
Accepted 11th January 2024

DOI: 10.1039/d3dt03178k

rsc.li/dalton

O–O bond formation *via* radical coupling in a dinuclear iron water oxidation catalyst with high catalytic activity†

Ge Li and Mårten S. G. Ahlquist *

The use of iron-based catalysts for the water oxidation reaction is highly attractive due to the high abundance of iron. While many molecular catalysts have been made, most show limited activity and short lifetimes. An exception with higher activity was presented by Thummel and co-workers in 2015. Herein we present a study on the feasibility of the coupling of two O centered radicals originating from the two subunits of the dinuclear catalyst. The reaction pathway includes the oxidation to the active species Fe^{IV}–O–Fe^{IV} but avoids further high potential oxidations which previous mechanistic proposals have relied on.

The realization of artificial photosynthesis capable of producing renewable energy is a promising approach to combat the climate crisis resulting from the high reliance on fossil fuels currently.[1] In the simplest form, artificial photosynthesis consists of the water oxidation reaction that generates O_2 and the proton reduction reaction that generates H_2. While H_2 is the product we use to store intermittent energy (*e.g.* solar energy) into chemicals, much focus has been on water oxidation since it is typically considered the bottleneck owing to the high thermodynamic requirement and sluggish kinetics.[2] Therefore, efficient catalysts are required to boost the water oxidation reaction. To investigate different reaction mechanisms that might potentially be applied to realistic heterogeneous catalysis, molecular water oxidation catalysts (MWOCs) are preferred due to their well-defined structures, flexible adjustable properties and informative characterization. Transition metals that can reach several accessible oxidation states are typically suitable for creating active MWOCs. Since the first well-characterized MWOC based on ruthenium was reported by Meyer's group in 1982,[3] extensive research studies have been conducted on Ru-based MWOCs, some of which possess high reaction rates with a turnover frequency (TOF) that exceeds that of the oxygen-evolving complex in photosystem II.[4–8] Discovering O–O bond formation mechanisms and isolating crucial intermediates are essential for the development of MWOCs.[9,10] In addition to the two well-known O–O bond formation mechanisms, *i.e.*, water nucleophilic attack (WNA) and interaction of two metal-oxo units (I2M), several other mechanisms were presented by Cao, such as bimolecular hydroxyl coupling (BHC), intramolecular hydroxyl coupling (IHC), intermolecular oxo/oxyl coupling (IOC) and redox isomerization (RI).[11] Recently, MWOCs containing first-row transition metals (*e.g.* Mn,[12,13] Fe,[14–16] Cu,[17,18] Co,[16,19,20] Ni[21,22]) have emerged to reduce the use of scarce noble transition metals. Among them, iron is the most attractive and promising candidate due to its abundance, low price, low toxicity, and its valence electronic structure resembling that of ruthenium,[23] which the most efficient MWOCs contain.[24] In 2010, Collins and Bernhard reported the first Fe-based MWOC, Fe-TAML (TAML = tetraamido macrocyclic ligand), with the most electron-deficient groups, which displayed a TOF of 1.3 s^{-1} at pH 0.7 driven by ceric ammonium nitrate (CAN).[25] After six years, a pentanuclear Fe complex with a TOF of 1400 s^{-1} was designed by Masaoka's group although its practical use was limited by the special operating environment of high concentration organic solvent and a high overpotential of 500 mV.[14] Its reaction mechanism was proposed as intramolecular radical coupling inside the pentanuclear core.[26] Masaoka also stated that O–O bond formation in an intramolecular fashion is a key feature for multinuclear structures.[27] Recently, Zhang and Liao have reported three dinuclear Fe-based MWOCs and the one with more axial rotational flexibility of two Fe-oxos in the O–Fe–O–Fe–O species showed higher catalytic activity owing to its larger possibility of intramolecular radical coupling.[28] In 2015, Thummel's group reported a highly efficient dinuclear Fe-based MWOC, $[(H_2O)–Fe^{III}–(ppq)–O–Fe^{III}–(ppq)–Cl]^{3+}$ (ppq=2-(pyrid-2′-yl)-8-(1″,10″-phenanthrolin-2″-yl)-quinoline), with a TOF of 2.2 s^{-1}.[15] This dinuclear catalyst worked under aqueous conditions at pH 1 driven by $Ce^{IV}(NH_4)_2(NO_3)_6$

Department of Theoretical Chemistry & Biology, School of Engineering Sciences in Chemistry Biotechnology and Health, KTH Royal Institute of Technology, 10691 Stockholm, Sweden. E-mail: ahlqui@kth.se

† Electronic supplementary information (ESI) available. See DOI: https://doi.org/10.1039/d3dt03178k

(CAN). Zheng and co-workers proposed a mechanism where the dinuclear Fe-based MWOC first decomposed into two mononuclear moieties and the two highly oxidized moieties (Fe^{V}=O) were then attacked by nucleophilic nitrate to form the O–O bond, which is the same as the mechanism that was previously proposed for a mononuclear Fe-based complex by Liao.[29,30] Here, we revisit this dinuclear Fe-containing complex and propose a different possible reaction mechanism for the O–O bond formation.

In the experimental study, complex **1** [Cl–Fe^{III}–O–Fe^{III}–OH_2]$^{3+}$ characterized by a crystal structure analysis was proposed to be the initial state of the catalyst (Fig. 1). The catalytic mechanism was proposed to be initiated in two steps. Complex **1** [Cl–Fe^{III}–O–Fe^{III}–OH_2]$^{3+}$ first undergoes a two-electron oxidation to generate [Cl–Fe^{IV}–O–Fe^{IV}–OH_2]$^{5+}$. Two protons are then transferred to the solvent along with an internal electronic rearrangement to obtain the reactive species [Cl–Fe^{III}–O–Fe^{V}=O]$^{3+}$ which was proposed to be the species forming the O–O bond.[15] However, the reduction potential to transfer two electrons in the above mechanism to generate complex **1** was calculated to be 2.18 V, which is much higher than the onset potential of the operating system. The calculated potentials reported in this study were against the Ag/AgCl reference electrode at pH 1 which was the same condition as the experiment. Consequently, we propose an alternative mechanism where complex **1** undergoes two proton coupled electron transfers (PCET) to produce complex **3** [Cl–Fe^{IV}–O–Fe^{IV}=O]$^{3+}$, and we expect that complex **3** is responsible for initiating the O–O bond formation while at the same time following the first-order kinetics with regard to the initial rate of O_2 evolution and the catalyst concentration.

The first PCET process for complex **1** was calculated to occur at 1.66 V to generate [Cl–Fe^{III}–O–Fe^{IV}–OH]$^{3+}$, as shown in Table S2.† Similarly, the second PCET process requires a potential of 1.44 V to generate complex **3** from **2**. The lower potential of the second oxidation indicates that the two steps occur simultaneously driven by a potential of 1.66 V, which reasonably matches the experimental onset potential of 1.25 V, given that the onset potential is typically considered lower than the exact limiting water oxidation potential.[30] We tested the possibility of a further oxidation step to [Cl–Fe^{IV}–O–Fe^{V}=O]$^{4+}$; however, it requires a potential of 2.15 V which is far too positive to be possible. After the two PCET processes, the O2–Fe1 bond distance increased to 1.98 Å from 1.74 Å, while the O2–Fe2 bond distance shortened to 1.67 Å from 1.84 Å, as indicated in Fig. 1. The uneven distribution of the μ-oxo between two Fe centers in complex **3** indicates the unequal bond strengths of O2–Fe1 and O2–Fe2. Next we will consider a viable reaction mechanism that consists of the decomposition of [Cl–Fe^{IV}–O–Fe^{IV}=O]$^{3+}$ into two subunits by chloride nucleophilic attack and radical coupling of two [Cl–Fe^{IV}=O]$^{+}$.

Fig. 2 shows the spin density distribution of complex **3** (O1: −0.99, Fe1: −1.04, O2: 0.69, Fe2: 1.31). Together with the longer bond distance of O2–Fe1 (1.98 Å) than that of O2–Fe2 (1.67 Å) compared with complex **1** or **2** shown in Fig. 1, it indicates that the unrestricted singlet complex **3** could be considered as a combination of two triplet Fe^{IV}=O units that are antiferromagnetically connected by the weakly coordinated O2–Fe1 bond. [Cl–Fe^{IV}–O–Fe^{IV}=O]$^{3+}$ has a 3+ charge and is likely to be surrounded by multiple counter ions to avoid too large charge separation, similar to [Cl–Fe^{III}–O–Fe^{III}=OH_2]$^{3+}$ which is accompanied by three Cl^{-} in its crystal structure. Consequently, Cl^{-} is more probable to attack the weaker O2–Fe1 bond to generate two identical triplet [Cl–Fe^{IV}=O]$^{+}$ subunits to initiate the O—O bond formation rather than to attack the O2–Fe2 bond. With the decrease of the Cl1–Fe1 distance from 4.89 Å (reactant) to 3.71 Å (transition state) and then to 2.40 Å (product), the O2–Fe1 bond was broken and two identical triplet [Cl–Fe^{IV}=O]$^{+}$ subunits were generated, as shown in Fig. 3. The activation and reaction Gibbs free energies of this chloride nucleophilic attack process are 19.9 and 5.6 kcal mol^{-1}, respectively. In addition, similar calculations on the other two nucleophiles nitrate and water attacking the O2–Fe1 bond were performed, respectively. The Gibbs energy barriers and reaction Gibbs free energies for nitrate attack are 22.4 and 11.8 kcal mol^{-1}, and for water attack, 23.2 and 11.7 kcal mol^{-1}. Both nitrate attack and water attack show higher energy barriers and reaction energies than the chloride attack, which supports the decomposition of complex **3** attacked by the chloride. For the stepwise dissociative pathway, the Gibbs

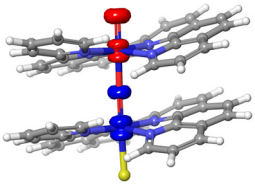

Fig. 2 Spin density distribution of complex **3** [Cl–Fe^{IV}–O–Fe^{IV}=O]$^{3+}$ at an isovalue of 0.05 electrons per bohr^{3}.

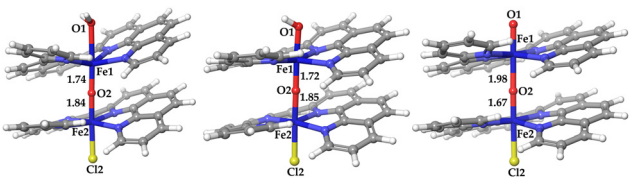

Fig. 1 Structures of complex **1** ([Cl–Fe^{III}–O–Fe^{III}–OH_2]$^{3+}$), **2** ([Cl–Fe^{III}–O–Fe^{IV}–OH]$^{3+}$) and **3** ([Cl–Fe^{IV}–O–Fe^{IV}=O]$^{3+}$). The values above and below are the bond distances of O2–Fe1 and O2–Fe2 in Å.

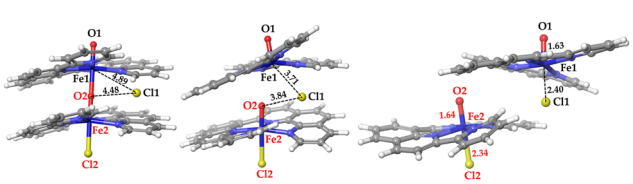

Fig. 3 Structures of the reactant (complex **4**), transition state (4TS) and product of [Cl–Fe^{IV}–O–Fe^{IV}=O]$^{3+}$ (4IM) attacked by one nucleophilic chloride ion. The unit of distance is Å.

energy required to directly split the O2–Fe1 bond was calculated to be 32.0 kcal mol^{-1}, which is much higher than that (19.9 kcal mol^{-1}) of the concerted dissociative mechanism assisted by chloride insertion. A similar decomposition of this dinuclear Fe-based MWOC *via* the water nucleophilic attack was proposed by Zheng's group. The activation and reaction Gibbs free energies were calculated to be 13.7 and 7.2 kcal mol^{-1} with the ωB97XD functional, using the LANL2DZ basis set for the Fe atoms and the 6-31G(d,p) basis set for other atoms. Hetterscheid and co-workers also experimentally suggested that a μ-oxo bridged dinuclear Fe-based MWOC is likely to be decomposed when oxidized to high valence states.[29,31]

The generation of two identical [Cl–Fe^{IV}═O]$^{+}$ subunits indicates the possibility of forming an O–O bond *via* the more efficient radical coupling pathway, similar to the Ru(bda)L$_2$ (bda^{2-} = 2,2′-bipyridine-6,6′-dicarboxylate, L is typically a nitrogen heterocycle) series of MWOCs.[32–34] The potential energy surface during the scan of the O–O bond distance from 4.09 Å to 1.20 Å at the antiferromagnetic open-shell singlet state ([Cl–Fe^{IV}═O···O═Fe^{IV}–Cl]$^{2+}$, triplet–triplet) is presented in Fig. 4. The structures of the reactant (O–O distance 4.09 Å), transition state (2.03 Å) and product (1.41 Å) are shown in Fig. 5, from which the electronic energy barrier and reaction energy are obtained as 13.2 and −7.4 kcal mol^{-1}, respectively. After taking solvation free energy and thermal corrections into account, the Gibbs free energies for activation and reaction are 12.1 and −8.6 kcal mol^{-1}, respectively.

The energy profile of the decomposition of complex **3** *via* chloride nucleophilic attack and the following radical coupling is presented in Fig. 6. These two processes are energy demanding with energy barriers of 19.9 and 16.4 kcal mol^{-1}, respectively. Although the energy barrier for the breakage of complex **3** is 19.9 kcal mol^{-1}, some effects, such as the explicit solvent effect, are not included to obtain more accurate values, which is challenging for this large complex. Moreover, the energy barrier of the similar decomposition *via* water nucleophilic attack in Zheng's computational study is 13.7 kcal mol^{-1}, which indicates that the activation energy of the decomposition attacked by nucleophiles in the solution could be as low as 13.7 kcal mol^{-1} and then the energy barrier for the whole process given in Fig. 6 will be 16.4 kcal mol^{-1}. Considering the accuracy of the chosen computational methods, both 19.9 and 16.4 kcal mol^{-1} are reasonable energy barriers that are within the range of 17.1 kcal mol^{-1} converted from the TOF value of 2.2 s^{-1}. Since the resting state of the investigated mechanism contains the same atoms as the transition state, it is expected to follow first-order kinetics.

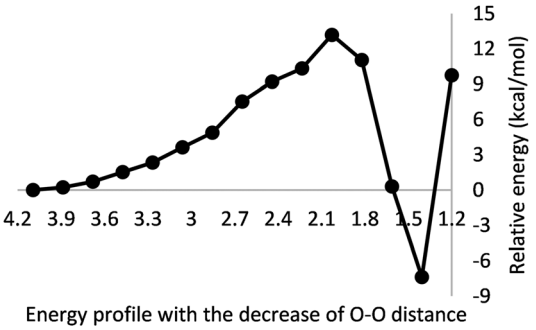

Fig. 4 Energy profile of the [Cl–Fe^{IV}═O]$^{+}$ dimer *via* the radical coupling pathway.

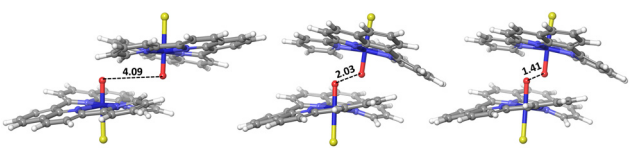

Fig. 5 Structures of the reactant (complex **5**), transition state (5TS) and product (5IM) of the [Cl–Fe^{IV}═O]$^{+}$ dimer *via* the radical coupling pathway after [Cl–Fe^{IV}–O–Fe^{IV}═O]$^{3+}$ was decomposed by chloride nucleophilic attack. The unit of distance is Å.

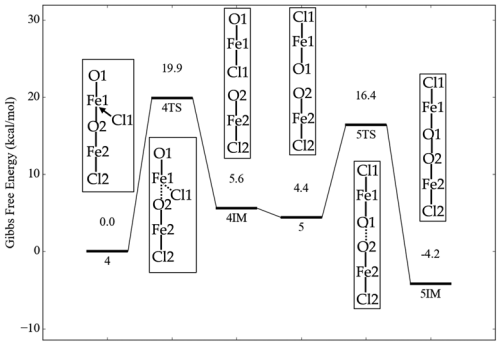

Fig. 6 Energy profile of decomposition of complex **3** and radical coupling of the [Cl–Fe^{IV}═O]$^{+}$ dimer.

This study proposed an alternative reaction mechanism for the efficient dinuclear Fe-based MWOC [(H$_2$O)–Fe^{III}–(ppq)–O–Fe^{III}–(ppq)–Cl]$^{3+}$. Unlike the already proposed mechanism where the decomposed mononuclear catalysts need to be oxidized to Fe^{V}═O species to evoke the O–O bond formation by nitrate nucleophilic attack, our mechanism shows that the dinuclear Fe-based MWOC only needs to undergo two PCET processes to generate [Cl–Fe^{IV}–O–Fe^{IV}═O]$^{3+}$ with a potential of 1.66 V *vs.* the Ag/AgCl reference electrode at pH 1. [Cl–Fe^{IV}–O–Fe^{IV}═O]$^{3+}$ then reacts with a Cl^{-} counter ion to break one of the Fe–O bonds generating two identical monomers. The O–O bond is then formed *via* the radical coupling pathway of the two Fe^{IV}═O species. The activation free energy for the decomposition to two monomers was calculated to be 19.9 kcal mol^{-1} and that for the O–O bond formation was calculated to be 16.4 kcal mol^{-1}, relative to the dinuclear complex. The calculated potentials, activation free energies, and first-order kinetics agree with the observed experimental data.

Conflicts of interest

There are no conflicts to declare.

Acknowledgements

This work was supported by Vetenskapsrådet (2022-04085) and the China Scholarship Council (201700260230). The computations were enabled by resources provided by the National Academic Infrastructure for Supercomputing in Sweden (NAISS) and the Swedish National Infrastructure for Computing (SNIC) at National Supercomputer Center (NSC, Linköping University) and PDC Center for High Performance Computing (PDC-HPC, KTH, Royal Institute of Technology) partially funded by the Swedish Research Council through grant agreements no. 2022-06725 and no. 2018-05973.

References

1 M. D. Kärkäs, O. Verho, E. V. Johnston and B. Åkermark, *Chem. Rev.*, 2014, **114**, 11863–12001.
2 B. Zhang and L. Sun, *Chem. Soc. Rev.*, 2019, **48**, 2216–2264.
3 S. W. Gersten, G. J. Samuels and T. J. Meyer, *J. Am. Chem. Soc.*, 1982, **104**, 4029–4030.
4 L. Duan, F. Bozoglian, S. Mandal, B. Stewart, T. Privalov, A. Llobet and L. Sun, *Nat. Chem.*, 2012, **4**, 418–423.
5 L. Wang, L. Duan, Y. Wang, M. S. G. Ahlquist and L. Sun, *Chem. Commun.*, 2014, **50**, 12947–12950.
6 R. Matheu, M. Z. Ertem, J. Benet-Buchholz, E. Coronado, V. S. Batista, X. Sala and A. Llobet, *J. Am. Chem. Soc.*, 2015, **137**, 10786–10795.
7 N. Vereshchuk, R. Matheu, J. Benet-Buchholz, M. Pipelier, J. Lebreton, D. Dubreuil, A. Tessier, C. Gimbert-Suriñach, M. Z. Ertem and A. Llobet, *J. Am. Chem. Soc.*, 2020, **142**, 5068–5077.
8 J. Yang, L. Wang, S. Zhan, H. Zou, H. Chen, M. S. G. Ahlquist, L. Duan and L. Sun, *Nat. Commun.*, 2021, **12**, 373.
9 T. Liu, G. Li, N. Shen, L. Wang, B. J. Timmer, S. Zhou, B. Zhang, A. Kravchenko, B. Xu and M. S. Ahlquist, *CCS Chem.*, 2021, 2612–2621.
10 C. Casadevall, V. Martin-Diaconescu, W. R. Browne, S. Fernández, F. Franco, N. Cabello, J. Benet-Buchholz, B. Lassalle-Kaiser and J. Lloret-Fillol, *Nat. Chem.*, 2021, **13**, 800–804.
11 X.-P. Zhang, H.-Y. Wang, H. Zheng, W. Zhang and R. Cao, *Chin. J. Catal.*, 2021, **42**, 1253–1268.
12 G. Maayan, N. Gluz and G. Christou, *Nat. Catal.*, 2018, **1**, 48–54.
13 J. Guan, Z. Duan, F. Zhang, S. D. Kelly, R. Si, M. Dupuis, Q. Huang, J. Q. Chen, C. Tang and C. Li, *Nat. Catal.*, 2018, **1**, 870–877.
14 M. Okamura, M. Kondo, R. Kuga, Y. Kurashige, T. Yanai, S. Hayami, V. K. K. Praneeth, M. Yoshida, K. Yoneda, S. Kawata and S. Masaoka, *Nature*, 2016, **530**, 465–468.
15 L. D. Wickramasinghe, R. Zhou, R. Zong, P. Vo, K. J. Gagnon and R. P. Thummel, *J. Am. Chem. Soc.*, 2015, **137**, 13260–13263.
16 H. Lv, X.-P. Zhang, K. Guo, J. Han, H. Guo, H. Lei, X. Li, W. Zhang, U.-P. Apfel and R. Cao, *Angew. Chem., Int. Ed.*, 2023, **62**, e202305938.
17 S. M. Barnett, K. I. Goldberg and J. M. Mayer, *Nat. Chem.*, 2012, **4**, 498–502.
18 Q.-F. Chen, Z.-Y. Cheng, R.-Z. Liao and M.-T. Zhang, *J. Am. Chem. Soc.*, 2021, **143**, 19761–19768.
19 Y. Wang, F. Li, X. Zhou, F. Yu, J. Du, L. Bai and L. Sun, *Angew. Chem., Int. Ed.*, 2017, **56**, 6911–6915.
20 N. Brodsky Casey, G. Hadt Ryan, D. Hayes, J. Reinhart Benjamin, N. Li, X. Chen Lin and G. Nocera Daniel, *Proc. Natl. Acad. Sci. U. S. A.*, 2017, **114**, 3855–3860.
21 L. Wang, L. Duan, R. B. Ambre, Q. Daniel, H. Chen, J. Sun, B. Das, A. Thapper, J. Uhlig, P. Dinér and L. Sun, *J. Catal.*, 2016, **335**, 72–78.
22 J. Lin, P. Kang, X. Liang, B. Ma and Y. Ding, *Electrochim. Acta*, 2017, **258**, 353–359.
23 G. Li and M. S. G. Ahlquist, *Dalton Trans.*, 2022, **51**, 8618–8624.
24 T. Liu, G. Li, N. Shen, L. Wang, B. J. Timmer, A. Kravchenko, S. Zhou, Y. Gao, Y. Yang and H. Yang, *Chem. – Eur. J.*, 2022, **28**, e202104562.
25 W. C. Ellis, N. D. McDaniel, S. Bernhard and T. J. Collins, *J. Am. Chem. Soc.*, 2010, **132**, 10990–10991.
26 R.-Z. Liao, S. Masaoka and P. E. M. Siegbahn, *ACS Catal.*, 2018, **8**, 11671–11678.
27 M. Kondo, H. Tatewaki and S. Masaoka, *Chem. Soc. Rev.*, 2021, **50**, 6790–6831.
28 H.-T. Zhang, X.-J. Su, F. Xie, R.-Z. Liao and M.-T. Zhang, *Angew. Chem., Int. Ed.*, 2021, **60**, 12467–12474.
29 S. Hu, P. Xu, R.-X. Xu and X. Zheng, *Inorg. Chem.*, 2021, **60**, 7297–7305.
30 Y.-Y. Li, L.-P. Tong and R.-Z. Liao, *Inorg. Chem.*, 2018, **57**, 4590–4601.
31 K. G. Kottrup, S. D'Agostini, P. H. van Langevelde, M. A. Siegler and D. G. H. Hetterscheid, *ACS Catal.*, 2018, **8**, 1052–1061.
32 S. Zhan, D. Mårtensson, M. Purg, S. C. L. Kamerlin and M. S. G. Ahlquist, *Angew. Chem., Int. Ed.*, 2017, **56**, 6962–6965.
33 S. Zhan, R. Zou and M. S. G. Ahlquist, *ACS Catal.*, 2018, **8**, 8642–8648.
34 L. Duan, C. M. Araujo, M. S. G. Ahlquist and L. Sun, *Proc. Natl. Acad. Sci. U. S. A.*, 2012, **109**, 15584.